# Active control of a backward facing step flow with plasma actuators

**Juan D'Adamo**[*] **Roberto Sosa** **Guillermo Artana**

CONICET. Facultad de Ingenieria. Universidad de Buenos Aires
Argentina

## ABSTRACT

*Active control over a backward-facing step flow is studied experimentally by means of plasma based devices. The Reynolds number based on the step height h is 1520. An electrohydrodynamic actuator (EHD), dielectric barrier discharge(DBD) type, is flush-mounted to the step wall. The DBD configuration adds momentum locally, normal to the separated shear layer thus producing strong modifications downstream. The actuation is periodic and its frequency and amplitude are scrutinized to characterize the flow behavior under forcing. Measures of velocity fields for these flows are obtained from particle image velocimetry (PIV). As reported by previous works, the reattachment length shows an important reduction for an optimum forcing frequency. This value closely matches the shear layer flow natural frequency. On the other hand, the flow is less sensitive to the forcing amplitude though the analysis allows us to optimize the actuation in order to save power consumption.*

## Nomenclature

EHD Electrohydrodynamic.

BFS Backward facing step.

---

[*] Correspondence author jdadamo@fi.uba.ar

$Re$ Reynolds number.

$U_\infty$ Upstream free flow velocity.

$h$ Backward facing step height.

$x, y, z$ Streamwise, transversal and spanwise spatial coordinates.

$\Delta x$ PIV spatial resolution.

$x_r$ Recirculation bubble length.

$H$ Channel height.

$W$ Channel width.

$E_r$ Expansion ratio.

KH Kelvin Helmholtz.

$f_S$ Pitot measures sampling frequency.

$\theta$ Momentum thickness.

$\delta_\omega$ Vorticity thickness.

$f_f$ Forcing frequency.

$St$ Strouhal number, $St = fh/U_m$.

$f_{EHD}$ Frequency of the DBD signal.

$T_{EHD}$ Period of the DBD signal.

$DC\%$ Electrical Duty cycle.

$T_{Burst}$ Burst period to modulate the DBD signal.

$T_{ON}$ Time corresponding to DBD signal operating.

$G$ DBD induced flow rate.

$U_j$ DBD induced jet velocity.

$u_x, u_y, u_z$ Streamwise, transversal and spanwise velocity components.

$U$ Velocity modulus: $U = \sqrt{u_x^2 + u_y^2}$.

$\bar{()}$ Time average operator, i.e. $\bar{u}_x = 1/T \int_0^T u_x dt$.

$U_1, U_2$ Streamwise velocity for two uniform streams in a pure shear layer problem.

$U_m$ Mean streamwise velocity for two uniform streams in a pure shear layer problem, $U_m = (U_1 + U_2)/2$.

$\Delta U$ Streamwise velocity differ for two uniform streams in a pure shear layer problem, $\Delta U = U_1 - U_2$.

$R$ Velocity ratio for two uniform streams in a pure shear layer problem, $R = \Delta U/(2U_m)$.

$L_\omega$ Length scale accounting for vorticity thickness spatial changes.

$\Psi$ Eigenfunction associated to the Rayleigh equation.

$k$ Wavenumber $k = k_r + ik_i$.

$\omega$ Complex frequency $\omega = \omega_r + i\omega_i$.

$f_n$ Natural frequency issued from Rayleigh equation $f_n = \omega_r/2\pi$.

$f^+$ Non dimensional forcing frequency $f^+ = f_f/f_n$.

$Q$ Second invariant of $\nabla \boldsymbol{u}$.

$\Omega$ Vorticity.

$\lambda$ Wavelength of the wave perturbation $\lambda = U_m/f_f$

## 1 Introduction

Separated flows appear in many examples in nature and engineering systems. Study and control of separation phenomena has been addressed in the fluid mechanics community in the past decades. In particular, the flow over a backward facing step (BFS) represents a prototype of separated flows because of its simple geometry (see Fig. 1(a)) and the fact that the separation point is fixed. The Reynolds number ($Re$) may be defined with the upstream velocity $U_\infty$ and the step height $h$. The flow is initially stationary for low $Re$, where diffusion dominates ($Re < 750$). A recirculation bubble region develops and its length $x_r$ grows linearly with $Re$(Armaly et al., 1983). As studied by Thangam and Knight (1989), the factor of proportionality depends on the expansion ratio $E_r = (H-h)/H$, where $H$ is the height of the channel. Complex behaviour of the reattachment phenomena arises from a global three dimensional centrifugal instability (Barkley et al., 2002; Beaudoin et al., 2004) which takes place at moderate Reynolds numbers up to $\approx 750$. For greater $Re$ numbers ($> 1200$), the Kelvin Helmholtz(KH) instability becomes the predominant mechanisms for flow destabilization due to the increase of the thickness of the shear layer. The velocity gradients in the $y-$direction generate a vorticity sheet that eventually rolls-up to produce the characteristic vortex shedding of this kind of instability. This phenomenon is similar to the free mixing shear layer flow and share some features of its dynamic behavior as studied by Troutt et al. (1984). The proper scales of the flow are the momentum thickness ($\theta$) or the vorticity thickness $\delta_\omega$ rather than the step height $h$, as pointed out by Hasan (1992).

On the other side, another unsteady phenomenon called flapping motion was reported by several researchers (see a comprehensive discussion by Spazzini et al. (2001)). First reported by Eaton and Johnston (1982), the flapping motion is a low frequency instability that is associated to the oscillation of the recirculation bubble length.

Many works have addressed the problem of controlling separated flows. Actuators include: sound waves (Bhattacherjee et al., 1986), used to force locally (Chun and Sung, 1996); synthetic jets studied experimentally (Yoshioka et al., 2001; Yamada et al., 2011) or numerically (Dandois et al., 2007; Mehrez et al., 2010); inlet flow fluctuations studied in (Tihon et al., 2010); use of vortex generators (Duriez et al., 2006), etc. Even for turbulent flow, the vortex structures generated by the KH instability persist and it is then suitable to focus a control action on them. Some authors agree (Bhattacherjee et al., 1986; Chun and Sung, 1996; Yoshioka et al., 2001) on the fact that forcing at KH frequency enhances flow mixing and major reductions on the recirculation bubble length, even for turbulent regimes. But as pointed out by Dandois et al. (2007), in their investigation of the separated flow in a ramp geometry, there are some differences reported on the most effective forcing Strouhal number $St = f_f \ell / U_\infty$, where the forcing frequency is non-dimensionalized with a velocity $U_\infty$ and a characteristic length $\ell$, i.e. the step height $h$, the vorticity thickness $\delta_\omega$ or the momentum thickness $\theta$. A study of BFS flow forced in a wide range of frequencies around the KH values and with different forcing amplitudes seems to be lacking.

Flow control EHD actuators have received special attention over the last years, as reviewed by Moreau (2007) or Corke et al. (2010). Most of these actuators use non-thermal surface plasmas in which the air flowing close to the surface of the body is weakly ionized. Due to the presence of charged particles within a highly non-uniform electric field and through a collisional mechanism, the plasma can create a body force near the electrode surface (Boeuf et al., 2007). Consequently, a flow can be superimposed without adding mass through this momentum coupling mechanism. The plasma actuators are technologically attractive because of their simplicity (they have no moving parts), their spanwise homogeneity, the very short response time (typically of the order of milliseconds) and their low energy consumption. In addition, by means of burst modulation, the plasma actuators allow a relatively easy adjustment of the actuation control parameters (amplitude and frequency) (Benard and Moreau, 2010). Most of the studies with plasma actuators in the last decade have been undertaken considering a dielectric barrier discharge

(DBD) which was perfected for the first time in air at atmospheric pressure by Masuda and Washizu (1979) for ionic charging of particles. Roth et al. (1998) used it for airflow applications at the end of the 1990s, characterizing the injected momentum for a flat plate and airfoil flows. DBD actuators have also been applied in the control of bluff body flow as in (Thomas et al., 2006; Jukes and Choi, 2009; Sosa et al., 2011; D'Adamo et al., 2012). In these kinds of devices, the discharge is produced by applying a high voltage ac signal to a pair of electrodes that are separated by a dielectric layer. Typically, the voltage magnitude is a few kilovolts, the ac frequency is between 100 Hz and 10 kHz, and the dielectric layer is of thickness 0.1-1 mm. Under these conditions, stable surface plasma, consuming tens of watts per meter of electrode, can be easily created at atmospheric pressure (Moreau, 2007; Corke et al., 2010).

Our aim in this study is to use a plasma actuator to analyze the separated forced flow in a regime in which transition to turbulence depends mainly on KH instability. The geometry of BFS with a fixed point for flow separation simplifies the study. Although the flow may present three dimensional structures (Lanzerstorfer and Kulhmann, 2012) the main instability that develops it is a 2D KH. Furthermore, the 2D excitation that we perform reduces its spanwise variations as it happens in other separated flow problems (Naim et al., 2007).

We intend with this work to characterize this kind of flow when it is forced by a plasma actuator. This would be the necessary benchmark in order to design closed-loop actuation for which this kind of actuator is an attractive device as it does not need moving parts and forcing amplitudes and frequencies can be easily operated from output signals of the flow. Furthermore, if the flow behaves linearly for some range of actuation, this would be an useful feature to start dealing with future closed-loop design.

## 2 Experimental Setup

### 2.1 Flow geometry

The experiment takes place in a low-speed closed wind tunnel whose upstream flow velocity $U_\infty$ ranges from 0.2 to 2 m/s. As showed in Fig. 1(a), the cross section is square, width $W$ and height $H$ both of 180 mm length downstream the step. The the BFS has a step height $h = 20$ mm thus the expansion ratio $E_r$ is $H/(H-h) = 1.14$. $H$ is constant 1.60m downstream the step and upstream the step $H-h$ is constant over 0.8m.

Quantitative measurements were carried out using 2D particle image velocimetry (PIV) on a vertical plane placed at mid-span of the BFS. The trajectories of the seeding particles and those of the fluid particles surrounding the tracer have frequently been considered to be the same in flow visualizations by smoke injection techniques and in PIV experiments. However, if a slipping velocity is verified between the tracer and the fluid, the trajectories might differ. The tracer particles could "swim" in the moving media, and the information obtained from the tracers must be carefully examined. In our experiments the flow is seeded with olive oil droplets, produced by a LaVision V-Z Droplet seeder, with a mean droplet diameter of 1 micron. As analyzed in a previous article (Artana et al., 2002), the influence of coulombic forces on the tracer trajectory when using seeding particles of this size can be disregarded without introducing a significant error.

Image acquisition and PIV calculations were performed using a LaVision system, composed of an ImagerPro 1600 × 1200 CCD camera with a 14-bit dynamic range capable of recording double-frame pairs of images at 16 Hz and a two-rod Nd:YAG (15 mJ) pulsed laser synchronised by a customised PC using LaVision DaVis 7.1 software. The laser sheet width was about 1 mm in the test section, located at the middle of the spanwise length of the channel $z = 0$. The entire 150 mm × 75 mm imaging region gives a spatial resolution of $\Delta x = 0.0375h$. An identical camera was added when we needed to enlarge the field of vision in order to characterize longer recirculation bubbles. Additional measures were taken at $z = \pm W/4$ in order to verify the 2D assumption.

Concerning PIV uncertainties, a conservative value can be calculated as follows. The system resolution for distances can be estimated as the product of the pixel resolution ($1/4$ pix) and the pixel size (see i.e. Hart (2000) for a study on PIV uncertainties). In that way, the resolution of the velocity field can be estimated dividing the latter value by the time between a pair of laser pulses. For the selected case to be controlled, this time value is $3000\mu$s. In our case the pixel size was about 0.093 mm, leading to a conservative value of uncertainty

$$\Delta u = \frac{1}{4}\text{pix}0.093\frac{\text{mm}}{\text{pix}}\frac{1}{1500\mu\text{s}} = 0.03m/s$$

A Valydine differential pressure transducer with an acquisition frequency up to $f_S$=100 Hz was used to acquire velocity fluctuations from a Pitot probe schematically showed in Fig. 1(a). The probe is placed at $x/h = 4, y/h = 0.5, z = 0$.

Further post-processing and analysis were done using Scientific Python environment.

## 2.2 DBD Plasma actuator

The plasma actuator consisted of an asymmetric dielectric barrier discharge (DBD) flush mounted on the vertical wall of the BFS as is shown in Fig. 1(a). The scheme of the electrodes is more detailed in Fig. 1(b). This wall (thickness 1 mm) was used as a dielectric barrier for the electrodes of the DBD discharge. The DBD consisted of a pair of flat aluminum-foil electrodes (50 $\mu$m thickness, spanwise length 180 mm) oriented perpendicular to the mean flow direction.

The electrode exposed to the air (electrode (1)) was connected to the output of an AC power supply (peak-to-peak voltage $V_{AC}$ in the range 0 - 20 kV) and the encapsulated electrode (electrode (2)) was grounded. Hence, the plasma actuator induces an ionic wind flow as sketched on Fig. 1(b). The AC power supply consisted of a function generator coupled to an audio-amplifier (of 700W) that fed a high voltage transformer coil. In practice there was an optimal matching frequency, established by the resonance between the transformer inductance and the stray capacity of the electrode arrangement, including the wire connections. For our circuit geometry, the optimum excitation AC frequency was $f_{EHD} = 9kHz \quad (T_{EHD} = 1/f_{EHD} = 111\mu s)$.

The signal generator can operate the DBD by a $T_{Burst}$ periodic burst modulation, of the sinusoidal high voltage signal. The forcing frequency is then $f_f = 1/T_{Burst}$. On the other hand, the effect of the duty-cycle ($DC\%$ defined as: $100 \times (T_{ON}/T_{Burst})$ being $T_{ON}$ the time during which the plasma is produced, see Fig. 1(c)) was explored for values from 25 % up to 75 %. This parameter quantifies the fraction of time that the discharge, and consequently the forcing, is active. In this way, by changing this parameter, it is possible to modify the time averaged intensity of actuation.

It is important to quantify the strength of the forcing plasma to describe the effectiveness of the flow control device. It is customary to use a combination of plasma voltage and current applied to the plasma actuator as an indicator of plasma forcing (Sosa and Artana, 2006). However the relationship between the voltage and current applied to the plasma actuator and the force being generated is not unique. The plasma force is also a function of the current wave form, dielectric material, geometry of plasma actuator, as well as the operating environment such as temperature, pressure, and humidity (Moreau, 2007). Also, some authors looking for analogies with actuation with synthetic jets have proposed the use of a momentum coefficient, which uses the time averaged momentum flow incorporated by the actuator and the free-stream momentum flow through a cross section of the body (Jukes and Choi, 2009).

In the present work, the momentum introduced by the DBD actuator produces a jet whose velocity at close vicinity of the wall cannot be determined directly by PIV due to reflections and high velocity gradients. Though we cannot properly determine a momentum coefficient, nevertheless, an indirect measure, allows us to estimate the relative intensity of the actuation between the different *DC* values. Fig. 2 shows a typical time averaged flow field when the plasma actuator is applied in quiescent air. For each considered *DC* value we have calculated the induced flow rate through the horizontal plane $y/h = 1.5$. As is shown in Table 1, for increasing *DC* values, the induced flow rate $G$ augments. In order to roughly determine the flow velocity near the actuator we have estimated a jet of width $0.25h$ at $y/h = 0.25$. Thus, at this location the generated jets have velocities $U_j$ in a range $0.13U_\infty < U_j < 0.35U_\infty$ for the range of *DC* values.

## 3 Non forced flow

### 3.1 Mean flow

In order to characterize the flow on the non-forced case, a range of Reynolds $500 < Re < 2600$ is explored. As an example, we show in Fig. 3 contours of the mean non-dimensional velocity modulus $U/U_\infty$ and streamlines for the mean flow at $Re = 1520$. Mean (temporal averaged) values are determined from ensembles of 780 snapshots. This number of measured fields, taken at random sampling, was found to be sufficient for the convergence of the averaged field. On the other hand, additional sets of measures were taken at $z = \pm W/4$. These measures are similar to those at $z = 0$, verifying the flow bidimensionality at this regime when forcing.

Contours of the velocity modulus as well as streamlines are used to represent the flow. The recirculation bubble manifests from the streamlines and its length $x_r$, the distance between the step corner and the point of reattachment on the bottom wall, is a typical measure for the BFS flow. This point is characterized by a time-averaged zero streamwise velocity $\bar{u}_x \simeq 0$ close to the bottom wall, $y \simeq 0$. In order to determine $x_r$, we made use of the contours of the average velocity for positions $y/h = 0.0375$. Values between $\bar{u}_x = 0 \pm 2\Delta u$ define $x_r$.

Figure 5 shows the evolution of $x_r$ as a function of $Re$ for unforced cases in our configuration. This evolution is similar to previous works i.e. (Armaly et al., 1983) where three distinct regions are defined. First, $x_r$ increases for laminar regimes up to $Re \sim 800$ (this low $Re$ numbers regime was not extensively explored in this work). For higher Reynolds numbers (in our case, $800 < Re < 1520$) the KH instability develops and the recirculation length decreases. The flow is still laminar at the separation edge as our data follows the Blasius solution for laminar boundary layer. Finally, the recirculation region reaches an asymptotic value ($4h < x_r < 6h$ for our configuration), when turbulence is fully developed. We selected the case $Re = 1520$, $x_r \simeq 5.70h$, far enough from the laminar regime, because we are interested in controlling flows with transition to turbulence behavior.

### 3.2 Natural frequency

In order to determine the natural frequency $f_n$ for the unforced flow we placed the Pitot probe at $x/h = 4, y/h = 0.5, z = 0$ in order to acquire $u_x$ fluctuations. We measure 20 sets of 2000 samples. Although for each set the frequency resolution results $\Delta f = f_S/(2n_{samples}) = 0.025$, the absolute error was determined base on the mean standard deviation. Hence we adopted as the frequency measurement uncertainty $\Delta f = 0.1$ Hz. The power spectrum for $u_x$ is estimated from the resulting signal as showed in Fig. 6. We observe a range of frequencies $8.5 < f < 11.5$Hz that is amplified by the shear layer, a peak about $f = 9.9$Hz is distinguishable after smoothing. It's worth mentioning that due to the frequency sampling rate of our PIV system, this value cannot be estimated directly from images. This frequency corresponds to the KH vortex passage. Indeed, for the pure shear layer that develops from two uniform streams of respective velocities $U_1$ and $U_2$, according to Ho and Huerre (1984), the frequency for the KH instability evolves related to the momentum thickness $\theta$ and mean velocity between the streams $U_m$ determined immediately downstream the separation point $x = 0$.

$$f_n[Hz] = 0.032\,(U_m(x=0)/\theta(x=0)) \tag{1}$$

where the momentum thickness θ is computed by:

$$\theta = \int_{-\infty}^{\infty} \left[ \frac{1}{4} - \left( \frac{\bar{u}_x(y) - \bar{U}_m)}{\Delta U} \right)^2 \right] dy \tag{2}$$

given the mean velocity $U_m = (U_1 + U_2)/2$ and $\Delta U = (U_1 - U_2)$ the velocity difference.

For our flow configuration, we estimate $U_1$ and $U_2$ as follows. First we consider a $x$ fixed position that determine a velocity profile $u_x$ which is correspondingly time averaged $\bar{u}_x$. The profiles, depicted in Fig. 4 are characterized by the free stream velocity $U_1$, far from the shear layer and the inner velocity that develops in the recirculation region in opposite sense. We define $U_2$ as the maximum value of this inner velocity. From our PIV results we have found for $x/h = 0$ that $\theta = 0.087h$ and $U_m(x/h = 0) = 0.57\ m/s$, thus the natural frequency is $f_n = 10.48$Hz which can be consider close to that measured with the Pitot probe. A Strouhal number based on θ, $St_\theta = f_n \theta / U_m = 0.0153$, is consistent with previous studies on the BFS flow (Eaton and Johnston, 1982; Hasan, 1992; Dandois et al., 2007).

Another useful tool to analyze KH instability and the receptivity of this separated flow to different excitation frequencies is to perform linear stability analysis (Michalke, 1965). If we analyze the mean flow fields, we may perform a local linear stability analysis for the two-dimensional free shear layer that develops from the separation edge.

Before undertaking such study, our data must satisfy the velocity profile shape and the weakly non parallel flow condition. According to inviscid linearized theory the smooth hyperbolic-tangent velocity profile, provides the basic flow which has been reviewed in (Ho and Huerre, 1984; Huerre and Rossi, 1998) and throughly studied (Michalke, 1964, 1965; Monkewitz and Huerre, 1982).

Figure 4 presents experimental data profiles fitted with $U_m\left[1 + R(\tanh(2y/\delta_\omega + \eta)\right)]$ with $R$ the velocity ratio $R = \Delta U/(2U_m)$ and η represents the inflexion point displacement of the velocity profile. The flow is made non-dimensional with mean velocity $U_m$ as a velocity scale and the half vorticity thickness $\delta_\omega/2$ as a length scale. We determine $\delta_\omega(x) = (U_1 - U_2)/(d\bar{u}_x/dy_{\max})$ by fitting the velocity profiles. There is very good agreement for each location $x$ from the backward-step, the main inviscid instability is therefore captured. When the flow approaches the bottom wall $y = -h$ we expect to deviate from such inviscid velocity profile.

Non parallel effects are considered negligible as a typical scale to take into account $L_\omega = [1/\delta_\omega)(d\delta_\omega/dx)]^{-1}$ is very small compared to the vorticity thickness $\delta_\omega$, $L_\omega/\delta_\omega < 0.08$ for $x/h < 3$. Hence, our experimental flow can be analyze within linear stability theory.

The linear stability of parallel shear flows can be studied from the incompressible inviscid Rayleigh equation:

$$(kU - \omega)\left(\frac{d^2\psi}{dy^2}\right) - k\frac{d^2\bar{u}_x}{d^2y} = 0 \tag{3}$$

where $\bar{u}_x$ is the time mean streamwise velocity, $k = k_r + ik_i$ the wavenumber, $\omega = \omega_r + i\omega_i$, the frequency and $\psi$ the eigenfunction associated. The boundary conditions for this equation are:

$$\psi(-\infty) = \psi(\infty) = 0 \tag{4}$$

The eigenvalue problem of the Rayleigh equation provides a dispersion relation $\mathcal{D}(k,\omega,R) = 0$. We solve equation (3) for each $x$ using a Chebyshev spectral collocation method. We study the spatial stability characteristics as our results shows spatially growing instabilities. To do so, we determine from our PIV measures the velocity ratio $R$ and vorticity thickness $\delta_\omega$ for each location $x$ as represented in Fig. 7(a) and 7(b). Vorticity thickness evolution characterize the development of the wave instability that precedes a vortex formation ($0 < x/h < 3$). Once the vortex is formed and convected ($x/h > 3$), the vorticity thickness grows linearly (Ho and Huang, 1982).

For a range of real frequencies $\omega$ we determine the mode $\psi(y)$ most amplified, Fig. 7(c), associated with an eigenvalue $k = k_r + ik_i$ that has the maximum growth rate $-k_i$ . Thus, we determine the corresponding frequency $f_n = \omega_r/(2\pi)$ and we obtain a local frequency for each value of $R$. The resulting frequency is presented in dimensional form scaling with $U_m$ and $\delta_\omega$ in Fig. 7(d). As $U_m$ decreases and $\delta_\omega$ augments, $f_n$ is expected to decrease from the separation point $x = 0$. The local selected frequency is nearly constant for the interval $2 < x/h < 3$ where its mean value is $f_n = 9.8$Hz, close to the Pitot measured value 9.9Hz. We consider this value to be the KH natural instability frequency, the linear stability analysis gives a practical method to evaluate the natural frequency from time averaged velocity profiles. Figure 7(d) shows that high frequencies may be amplified near the separation point. On the other hand, the BFS flow is receptive to lower frequencies further downstream, when it approaches the reattachment point, and it loses parallelism.

## 4 Forced flow

Once the natural frequency is established, we set the forcing frequencies of the DBD actuator to be evaluated. According to many authors (Bhattacherjee et al., 1986; Chun and Sung, 1996; Yoshioka et al., 2001; Wengle et al., 2001; Mehrez et al., 2010), an important reduction of the recirculation length is obtained when forcing the shear layer at the natural frequency. We explore, therefore a range of frequencies from 1Hz up to 34Hz for three forcing amplitudes. The non-dimensional excitation frequency defined as $f^+ = f_f/f_n$, has therefore a range $0.1 < f^+ < 3.4$.

### 4.1 Mean flow

The experimental mean fields were obtained by PIV measurements of the flow, averaging 780 instantaneous velocity fields. Figure 8 depicts the BFS flow behavior as a function of the forcing parameters for 81 tests. The curves show how $x_r$ depends on the forcing frequency rather than its amplitude. We performed 20 PIV sets of 780 snapshots for the selected non-forced case, $Re = 1520$, in order to have a statistic estimation of the uncertainty of $x_r$. The value is $2.85\text{mm} = 0.143h =$ which we bound to $4\Delta x = 0.15h$. The reference value is thus $x_r/h = 5.70 \pm 0.15$ and we extended the uncertainty to all forced cases.

We confirm that a major reduction, up to 35%, of the recirculation length takes place for forcing frequencies around the natural frequency. A global minimum of $x_r$ is appreciable in all three forcing amplitudes. We present the study of the mean flow modifications as a function of the forcing frequency in Fig. 9 for a fixed amplitude (DC=50%). We confirm that the forcing frequency has an important impact on the recirculation bubble shape. It is well known that within this recirculation bubble there are two distinct mean statistic flow structures (Hall et al., 2003): a large, or primary vortex region and a corner, or secondary counter-rotating vortex region. The plasma forcing modifies both of them, as we can observe on the streamlines in Fig. 9 compared to Fig. 3. The corner vortex gets closer to the step and is deformed by the plasma forcing, however, more PIV resolution would be necessary in order to accurately describe this structure evolution. We restraint therefore our present study to the dynamics of the primary vortex and the mean recirculation bubble length.

For $f^+ \simeq 1$, Fig. 9(b) the recirculation region attains its minimum length as we observe from the streamlines. For a lower frequency ($f^+ \simeq 0.1$) Fig. 9(a), the reduction is less noticeable as the receptiveness of the shear layer at such frequencies takes place further downstream. On the other hand, higher frequencies ($f^+ \simeq 2.8$) do not produce reductions on $x_r$ but in Fig. 9(c) the modifications on the streamlines reveals the footprint of stretched primary vortex on the mean flow, as suggested by Chun and Sung (1996) and we discuss in Section 4.3.

Additionally, regarding Fig. 8, the flow seems to be also sensitive to $f^+$ near a sub-harmonic ($\simeq 1/2$) and also for the first harmonic ($\simeq 2$). This effect was also found in previous works for another kind of excitation devices (Chun and Sung, 1996; Mehrez et al., 2010). The amplitude seems to attain an optimum, as when exceeding $DC = 50\%$ the actuator performance slightly decays. We shall bring some insight to these aspects by studying some underlying mechanisms of the KH instability.

### 4.2 Momentum thickness

Momentum thickness ($\theta$), which is proportional to $\delta_\omega$, along with the local velocity determines the dynamics of the KH vortex, as pointed out in section (3.2). We focus on the modifications induced by the actuation on $\theta$ evolution downstream of the separation point $x = 0$.

Figure 10 presents momentum thickness development for natural flow and considering three forcing frequencies: for a fixed amplitude ($DC = 25\%$), a frequency close to the natural one, together with a lower and a higher frequency.

For the non forced case, momentum thickness evolves from the boundary layer to attain mixing layer behavior. From $x = 0$, we observe a slightly decrease of $\theta$ as the turbulent inflow takes some distance to become a shear flow dominated by a large scale two dimensional instability. Once the mixing layer is established, it becomes unstable at $x/h \sim 2.7$ and the momentum thickness grows monotonically with a slope that can be fitted by

$$\frac{d\theta}{dx} = 0.034R \qquad \text{with } R = \frac{\Delta U}{2U_m} \tag{5}$$

an expression determined experimentally by Browand and Troutt (1985) for free mixing layers. In our case, for $R$ evaluated at $x/h \simeq 3$ the slope value coincides as showed on Fig. 10. As we already observed the recirculation bubble length is for this case $x_r/h = 5.70$.

The forcing frequency modifies the growth starting point as well as the growth rate. For $f_f \simeq f_n$, we observe a steeper slope for $\theta$ starting at $x/h \sim 1.3$, a value for which the shear layer is receptive to $f_f$. The slope decreases to a value closer to the natural behavior at $x/h \sim 2.2$. It becomes clear that vortex are formed further upstream than in the natural case, explaining the observed large reductions of the bubble recirculation length, about 30% for this case.

When forcing with a lower frequency $f^+ \simeq 0.2$, we produce larger structures in the shear layer that enhance momentum exchange between the recirculation bubble and the free flow. However, these structures take longer distances to effectively perturb the shear layer thus resulting in a lower reduction of the recirculation length respect to $f^+ \simeq 1$. The evolution of $\theta$ for this forcing frequency is similar to the natural case but it starts at $x/h \sim 2$ achieving a recirculation length reduction of $\sim 0.7h$ which corresponds to a 13% reduction.

Higher frequencies, $f_f \simeq 2.8 f_n$ develop more important fluctuations near the detachment point, supporting the linear stability analysis that showed receptiveness to high frequencies. For $f_f \simeq 2.8 f_n$ we observe in Fig. 10 that even though $\theta$ has greater values than the natural case, the slope is smaller and the recirculation length do not differ appreciably respect to the non forced case. This type of forcing produces smaller vortex that do not contribute to the formation of larger structures. This determines that in some cases, the recirculation length is even greater than the non forced one.

Comparing forcing amplitudes, Fig. 11, we observe roughly an optimum for the control parameter $DC = 50\%$ as expending more energy ($DC = 75\%$) does not produce more reduction of the recirculation length. Increasing the forcing amplitude moves upstream the onset of the momentum thickness growth. Additionally, we observe that $\theta(x \simeq 0)$ increases with the forcing amplitude, probably caused by the intensity of the fluctuations provoked by the ionic wind. Regarding $DC = 50\%$ as an optimal forcing amplitude, we could consider that further increases of the forcing amplitude (DC=75%) produce fluctuations that do not participate on the KH instability. This effect has been observed in the context of blowing/suction actuation by Yoshioka et al. (2001).

### 4.3 Vortex structures.

Observation on momentum thickness can be reinforced by typical snapshots of the flow that reveal the structures involved. Vorticity contours are depicted in Fig. 12 along with some $Q$-contours. As in Jeong and Hussain (1995) vortex identification for planar flows can be achieved by means of positive $Q$, the second invariant of $\nabla \boldsymbol{u}$

$$Q = -\frac{1}{2}\frac{\partial u_i}{\partial x_j}\frac{\partial u_j}{\partial x_i} = \frac{1}{2}\left(\|\boldsymbol{\Omega}\|^2 - \|\boldsymbol{S}\|^2\right) \tag{6}$$

a scalar that represents the local balance between shear strain rate($\boldsymbol{S}$) and vorticity ($\boldsymbol{\Omega}$) magnitude. Vortex cores are therefore distinguishable when $Q > 0$.

Non forced flow presents the shear layer development until a vortex is formed. The formation length appreciated in Fig. 12(a) is in agreement with momentum thickness behavior. Indeed, the shear layer perturbations that lead to a vortex core formation are noticeable around $x \simeq 2.5h$. The structure grows until it reaches the bottom wall. Forced flow at natural frequency reduces strongly the necessary length for vortex formation as showed in Fig. 12(b). We can see from Fig. 10 that the point when momentum thickness start to growth linearly is just displaced near the separation point. A similar scenario is found in a pure shear flow forced with micro-jet actuators (Parezanovic et al., 2013). From hydrodynamical stability theory we can represent the vortex contours for a perturbation at $x = 0$. Vorticity fluctuations are derived from $\Omega' = \Omega'_r + i\Omega'_i = (k^2\psi - \psi'')$ and are superposed to base flow vorticity from the hyperbolic profile $\Omega_0 = R(1 - \tanh^2 y)$. Choosing a small disturbance magnitude $\varepsilon = 0.0005$ we can write an expression for the resulting spatially developing flow:

$$\Omega = \Omega_0 + \varepsilon \exp(-k_i x)\left[\Omega'_r \cos(k_r x - \omega_r t) - \Omega'_i \sin(k_r x - \omega_r t)\right] \tag{7}$$

In Fig. 13 we appreciate that vorticity produced by the most unstable mode evolves spatially from $x \simeq 2.5h$. The vorticity values are obtained using scales from our experiment: $\delta_\omega/2$ for length and $U_m$ for velocity. As vorticity contours attain the bottom wall around $x \simeq 5$, as well as presented in experimental results in 12(a), the simplified linear theory cannot be extended further downstream.

Given that linear stability analysis provides the description of the predominant instability structure (the one with the maximum growth rate), forcing with KH natural frequency enhances the growth of the natural unstable mode. Therefore, forcing actuation at KH frequency produces the optimum reduction of the recirculation bubble size. At the same time, relative small perturbations at this frequency are strong enough to produce modifications. We expect therefore the flow to be less receptive to forcing amplitude modifications, a behavior early described in Fig. 11.

Forcing the flow with higher forcing frequencies produces smaller size vortex near the detachment region as observed on Fig. 12(d) for $f^+ = 1.8$. Natural vortex are inhibited and the recirculation region might become even larger than in non-forced flow. Nevertheless, vortex merging appears in shear flows when several wavelengths of the perturbation wave ($\lambda = U_m/f_f$) are attained (Ho and Huang, 1982). This phenomena would explain a similar bubble recirculation length between the non-forced case and the higher frequencies forced cases, even though smaller vortices structures are created in the latter condition.

When forcing the flow with lower frequencies $f^+ < 1$, one might expect that higher wavelengths and lower amplification rate takes place according to Fig. 7(c). However this is not observed in Fig. 12(c) where for $f^+ = 0.5$ we see vortex structures that are similar to those of $f^+ = 1$. The linear instability theory fails to describe this situation.

First, the forcing signal is square-like so it contains the harmonic $f^+ = 1$(see i.e. Benard and Moreau (2010)) that becomes more amplified by the flow: $k_i \simeq 0.06$ for $f^= + 0.5$, $k_i \simeq 0.30$ for $f^+ = 1$ . On the other hand, a larger period may allow the formation of a natural vortex. The actuation is although not as effective as in $f^+ = 1$ as the vortex is formed further downstream and it reaches the bottom wall between $3 < x_r < 4$. Even if subharmonic forcing enhances vortex merging in shear flow (Ho and Huang, 1982), in this case, there is not enough distance to observe such phenomena: the separated flow reach the bottom wall after few wavelengths. Finally, for much lower forcing frequencies the flow becomes insensitive to the actuation and the natural behavior takes place.

## 5 Conclusions

Plasma-based, local periodic forcing have been studied experimentally for the flow over a backward-facing step at $Re = 1520$. Simple methods for the study such as the linear stability analysis of the mean flow and the evolution of the momentum thickness gave us some insight on the dynamics aspects of the flow dominated in this case by a Kelvin-Helmholtz instability.

Linear stability analysis is useful to explain main behavior of natural and forced flow, particularly for forcing at the natural frequency. Natural frequency is precisely selected and the spatial development of the shear layer and its relation with reattachment point is predicted within the linear framework.

We defined therefore optimum control parameters of the actuator in order to reduce the recirculation bubble length. Relative small injected momentum achieves reductions up to 37%. In this sense, the optimum forcing frequency is associated to KH instability. This forcing produces coherent 2D vortex that are generated upstream and grow faster than in the natural case.

On the other hand, we find that adding momentum saturates for increasing forcing amplitudes. Eventually, excessive amplitude forcing could introduce non-coherent perturbations which do not contribute to the main dynamics associated with KH instability.

We hope that this control scenario will allow future works to have a physical benchmark before performing closed loop control with DBD actuators.

## Acknoledgments

The authors acknowledge grants of the CONICET and of the University of Buenos Aires.

## References

B. F. Armaly, F. Durst, J. C. Pereira, and B. Schönung, 1983, “Experimental and theoretical investigation of backward-facing step flow,” Journal of Fluid Mechanics, 127, pp. 473–496.

S. Thangam and D. Knight, 1989, “Effect of the stepheight on the separated flow past a backward facing step,” Physics of Fluids A, 1(3), pp. 604–606.

D. Barkley, M. Gomes, G. M, and Hend, 2002, “Three-dimensional instability in flow over a backward-facing step,” Journal of Fluid Mechanics, 47, pp. 167–190.

J. F. Beaudoin, O. Cadot, J. L. Aider, and J. E. Wesfreid, 2004, “Three-dimensional stationary flow over a backward-facing step,” European Journal of Mechanics B-Fluids, 23(1), pp. 147–155.

T. R. Troutt, B. Scheelke, and T. R. Norman, 1984, “Organized structures in a reattaching separated flow field. Journal of Fluid Mechanics,” Journal of Fluid Mechanics, 143, pp. 413–427.

M. A. Z. Hasan, 1992, "The flow over a backward-facing step under controlled perturbation : laminar separation," Journal of Fluid Mechanics, 238, pp. 73–96.

P. G. Spazzini, G. Iuso, M. Onorato, N. Zurlo, and G. M. Di Cicca, 2001, "Unsteady behavior of back-facing step flow," Experiments in Fluids, 30(5), pp. 551–562.

J. K. Eaton and J. P. Johnston, 1982, "Low-frequency unsteadiness of a reattaching turbulent shear layer." in "*Proceedings of the 3rd International Symposium on Turbulent Shear Flow*," .

S. Bhattacherjee, B. Scheelke, and T. R. Troutt, 1986, "Modification of vortex interactions in a reattaching separated flow," AIAA Journal, 24(4), pp. 623–629.

K. B. Chun and H. J. Sung, 1996, "Control of Turbulent Separated Flow over a Backward - Facing Step by Local Forcing," Experiments in Fluids, 21(6), pp. 417–426.

S. Yoshioka, S. Obi, and S. Masuda, 2001, "Organized vortex motion in periodically perturbed turbulent separated flow over a backward-facing step," International Journal of Heat Fluid Flow, 22(3), pp. 302–307.

S. Yamada, K. Honami, S anda Okamoto, M. Motosuke, and H. Ishikawa, 2011, "Control of Backward Facing Step Flow in Low Reynolds Number (Reattachment Flow Control by Synthetic Jet Using Stability Analysis)," Transactions of the japan society of mechanical engineers, 77(775), pp. 680–688.

J. Dandois, E. Garnier, and P. Sagaut, 2007, "Numerical simulation of active separation control by a synthetic jet," Journal of Fluid Mechanics, 574, pp. 25–58.

Z. Mehrez, M. Bouterra, A. El Cafsi, A. Belghith, and P. Lequéré, 2010, "Active control of flow behind a backward-facing step by using a periodic perturbation," ARPN Journal of Engineering and Applied Sciences, 5(2), pp. 21–28.

J. Tihon, V. Penkavova, and M. Pantzali, 2010, "The effect of inlet pulsations on the backward-facing step flow," European Journal of Mechanics B-Fluids, 29(3), pp. 224–235.

T. Duriez, J. L. Aider, and J. E. Wesfreid, 2006, "Base flow modification by streamwise vortices, application to the control of separated Flows," in "*Proceedings of FEDSM2006*," Miami, USA.

E. Moreau, 2007, "Airflow control by non thermal plasma actuators," Journal of Physics D: Applied Physics, 40(3), pp. 605–36.

T. Corke, C. Enloe, and S. Wilkinson, 2010, "Dielectric Barrier Discharge Plasma Actuators for Flow

Control," Annual Review of Fluid Mechanics, 42, pp. 505–529.

J. P. Boeuf, Y. Lagmich, T. Unfer, T. Callegari, and L. C. Pitchford, 2007, "Electrohydrodynamic force in dielectric barrier discharge plasma actuators," Journal of Physics D: Applied Physics, 40(3), pp. 652–663.

N. Benard and E. Moreau, 2010, "Capabilities of the dielectric barrier discharge plasma actuator for multi-frequency excitations," Journal of Physics D: Applied Physics, 43(14), pp. 1–14.

S. Masuda and M. Washizu, 1979, "Ionic charging of very high resistivity spherical particle," Journal of Electrostatics, 6(1), pp. 57–67.

J. Roth, D. Sherman, and S. Wilkinson, 1998, "Boundary layer flow control with a one atmosphere uniform glow discharge surface plasma," in "*AIAA Meeting*," Reno, USA.

F. Thomas, A. Koslov, and T. Corke, 2006, "Plasma actuators for bluff body flow control," in "*AIAA Meeting*," San Francisco, USA.

T. N. Jukes and K. S. Choi, 2009, "Flow control around a circular cylinder using pulsed dielectric barrier discharge surface plasma," Physics Of Fluids, 21(8), pp. 1–12.

R. Sosa, G. Artana, N. Benard, and E. Moreau, 2011, "Mean lift generation on cylinders induced with plasma actuators," Experiments in Fluids, 51(3), pp. 853–860.

J. D'Adamo, L. M. Gonzalez, A. Gronskis, and G. Artana, 2012, "The scenario of two-dimensional instabilities of the cylinder wake under EHD forcing: A linear stability analysis," Fluid Dynamics Research, 44, pp. 1–20.

D. Lanzerstorfer and H. C. Kulhmann, 2012, "Global stability of the two dimensional flow over a backward-facing step," Journal of Fluid Mechanics, 693, pp. 1–27.

A. Naim, D. Greenblatt, A. Seifert, and I. Wygnanski, 2007, "Active Control of a Circular Cylinder Flow at Transition Reynolds Numbers," Flow Turbulence Combustion, 78(3-4), pp. 383–407.

G. Artana, J. D'Adamo, L. Leger, E. Moreau, and G. Touchard, 2002, "Flow control with electrohydrodynamic actuators," AIAA Journal, 40(9), pp. 1773–1779.

D. P. Hart, 2000, "PIV error correction," Experiments in Fluids, 29(1), pp. 13–22.

R. Sosa and G. Artana, 2006, "Steady control of laminar separation over airfoils with plasma sheet actuators," Journal of Electrostatics, 64(7), pp. 604–610.

C. M. Ho and P. Huerre, 1984, "Perturbed Free Shear Layers," Annual Review of Fluid Mechanics, 16(1), pp. 365–422.

A. Michalke, 1965, “On spatially growing disturbances in an inviscid shear layer,” Journal of Fluid Mechanics, 23(3), pp. 521–544.

P. Huerre and M. Rossi, 1998, “Hydrodynamic Instabilities in open flows,” in “*Hydrodynamics and Nonlinear Instabilities*,” Cambridge University Press, New York, USA, pp. 81–193.

A. Michalke, 1964, “On the inviscid instability of the hyperbolictangent velocity profile,” Journal of Fluid Mechanics, 19(4), pp. 543–556.

P. Monkewitz and P. Huerre, 1982, “Influence of the velocity ratio on the spatial instability of mixing layers,” Physics Of Fluids, 25(7), pp. 1137–1143.

C. M. Ho and L. S. Huang, 1982, “Subharmonics and vortex merging in mixing layers,” Journal of Fluid Mechanics, 119, pp. 443–473.

H. Wengle, A. Hupperz, G. Barwolff, and G. Janke, 2001, “The manipulated transitional backward-facing step flow: an experimental and direct numerical simulation investigation,” European Journal of Mechanics B-Fluids, 20(1), pp. 25–46.

S. D. Hall, M. Behnia, C. A. Fletcher, and G. L. Morrison, 2003, “Investigation of the secondary corner vortes in a benchmark turbulent backward-facing step using cross-correlation particle imaging velocimetry,” Experiments in Fluids, 35(2), pp. 139–151.

F. K. Browand and T. R. Troutt, 1985, “The turbulent mixing layer: geometry of large vortices,” Journal of Fluid Mechanics, 158, pp. 489–509.

J. Jeong and F. Hussain, 1995, “On the identification of a vortex,” Journal of Fluid Mechanics, 285(69), pp. 69–94.

V. Parezanovic, J. C. Laurentie, C. Fourment, L. Cordier, B. Noack, and T. Shaqarin, 2013, “Modification of global properties of a mixing layer by open/closed loop actuation,” in “*Eighth International Symposium on Turbulence and Shear Flow Phenomena*,” Poitiers, Futuroscope, France.

## List of Figures

2 Time averaged velocity modulus contours for the forcing jet produced by the DBD actuator ($f_f = 10Hz$, $DC = 50\%$). Induced flow rate $G$ has been calculated through the plane marked with the dashed line

3 Contour of the velocity modulus $U/U_\infty$ and streamlines for the non-forced mean flow for $Re$ =1520. The recirculation length $x_r \simeq 5.70h$.

4 Symbols: PIV mean velocity profiles $\bar{u}_x(y)$ for different positions $x/h$. Solid lines: Data is fit by $f(y) = c_1 + c_2 * \tanh(c_3 * y + c_4)$

5 Symbols • represent the recirculation region length for different $Re$ numbers for non-forced flow. Symbol ★ stands for the selected case to be controlled.

6 Dashed line: Power spectrum signal for $u_x$ estimated from a Pitot probe located at $x/h = 4$. Solid line: the same data smoothed

7 Linear Stability analysis on experimental mean flow for the non-forced case, at $Re = 1520$. The selected frequency in (d) $f_n = 9.8Hz$ matches the Pitot measures.

8 Recirculation bubble length $x_r$ modifications under actuation for three forcing amplitudes and a range of frequencies $0.1 < f^+ < 3.4$.

9 Evolution of the mean flow, represented by contours of the non-dimensional velocity modulus $U/U_\infty$ and streamlines. Different forcing frequencies are considered.

10 Momentum thickness evolution downstream. Non-forced case and three forcing frequencies for a fixed forcing amplitude (%DC=25). Dashed lines show the corresponding recirculation length for each case.

11 Momentum thickness evolution downstream. Non-forced case and three forcing amplitudes for a fixed forcing frequency $f^+ = 1$.

12 Instantaneous vorticity contours for the natural flow and three forcing frequencies for $DC$=50%. Some $Q$ contours (solid lines) identify the main vortex of the flow. Formation length is appreciable as well as an approximate measure for the wavelength $\lambda$

13 Instantaneous vorticity contours for the more unstable mode of the linear stability problem for the non forced case. Experimental scales $\delta_\omega$ and $U_m$ are used on equation (7).

## List of Figures

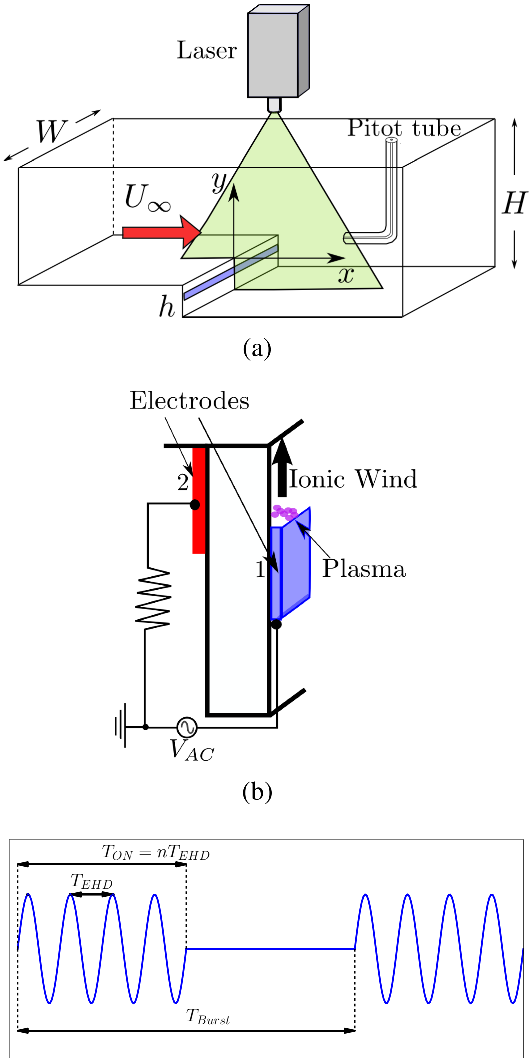

(a)

(b)

(c)

Fig. 1. (a) Outline of the test section geometry and position of the DBD actuator. The imaging region is represented schematically by the laser sheet (b) Detail of the DBD plasma actuator (c) Scheme of the burst modulation signal mode

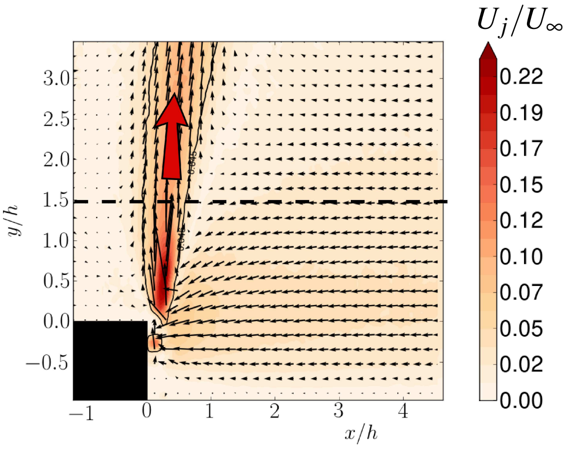

Fig. 2. Time averaged velocity modulus contours for the forcing jet produced by the DBD actuator ($f_f = 10Hz, DC = 50\%$). Induced flow rate $G$ has been calculated through the plane marked with the dashed line

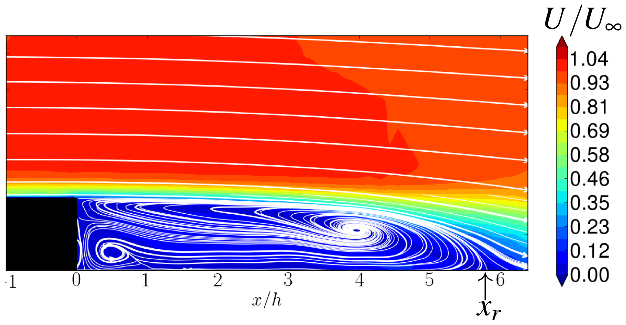

Fig. 3. Contour of the velocity modulus $U/U_\infty$ and streamlines for the non-forced mean flow for $Re$ =1520. The recirculation length $x_r \simeq 5.70h$.

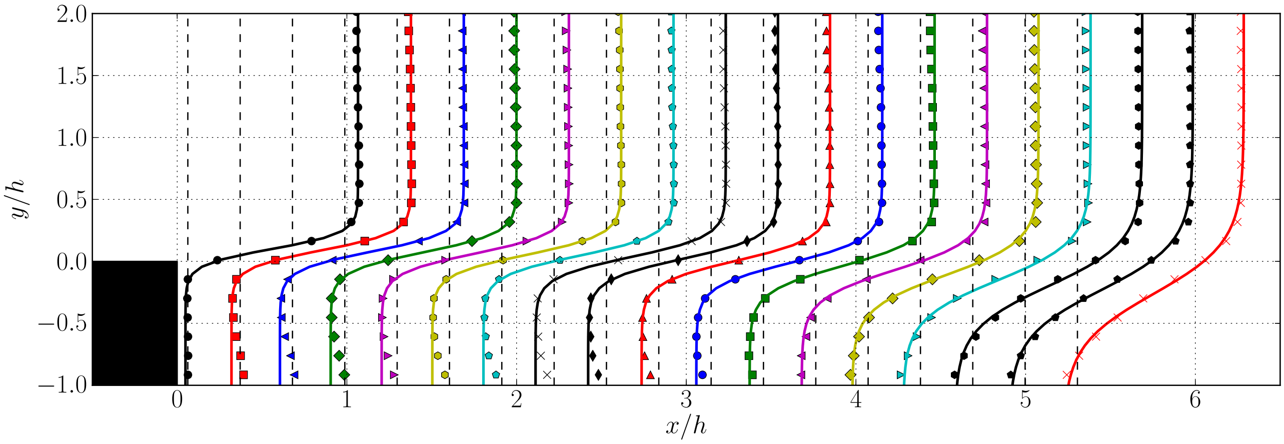

Fig. 4. Symbols: PIV mean velocity profiles $\bar{u}_x(y)$ for different positions $x/h$. Solid lines: Data is fit by $f(y) = c_1 + c_2 * \tanh(c_3 * y + c_4)$

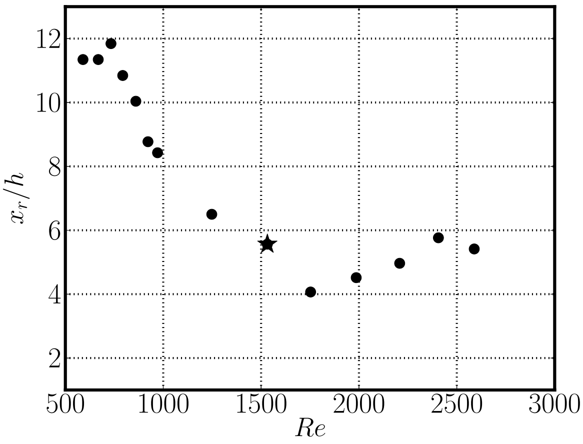

Fig. 5. Symbols ● represent the recirculation region length for different $Re$ numbers for non-forced flow. Symbol ★ stands for the selected case to be controlled.

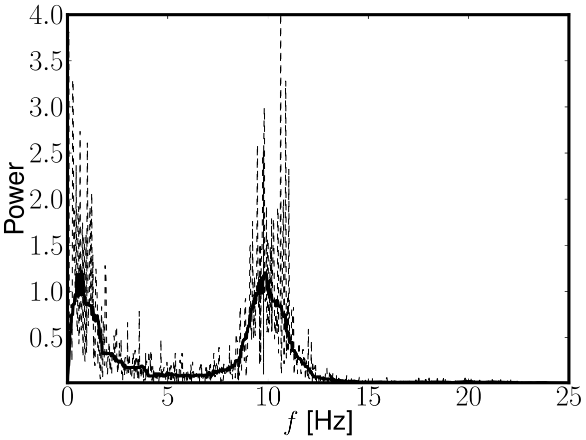

Fig. 6. Dashed line: Power spectrum signal for $u_x$ estimated from a Pitot probe located at $x/h = 4$. Solid line: the same data smoothed

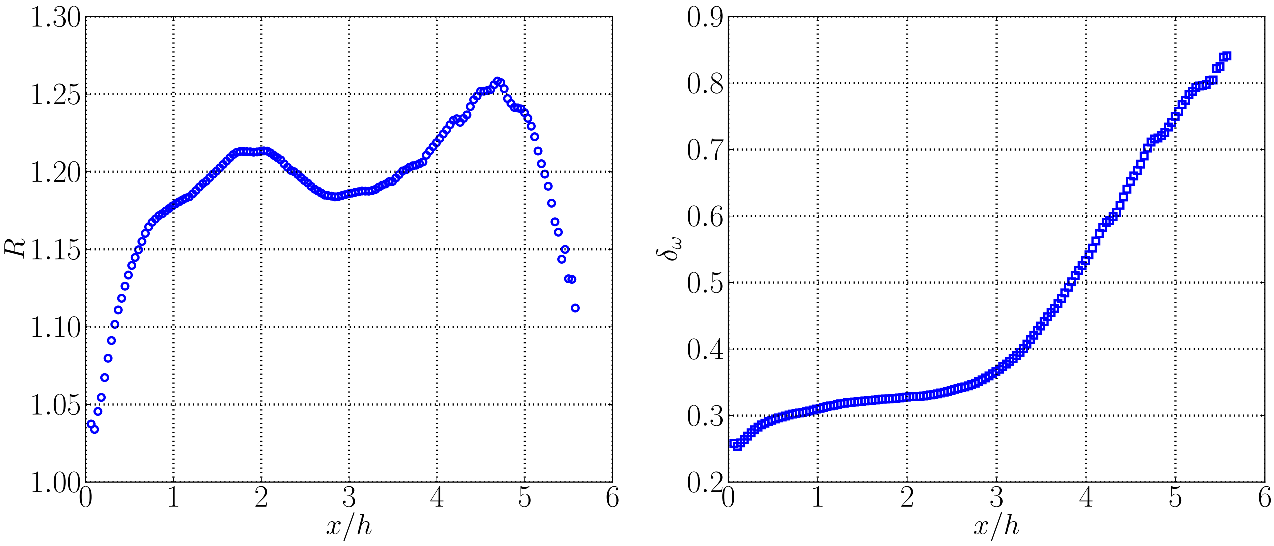

(a) Streamwise evolution of the velocity ratio $R$.

(b) Streamwise evolution of the vorticity thickness $\delta_\omega$. A linear behavior follows from $x \simeq 3$, where the natural frequency is selected.

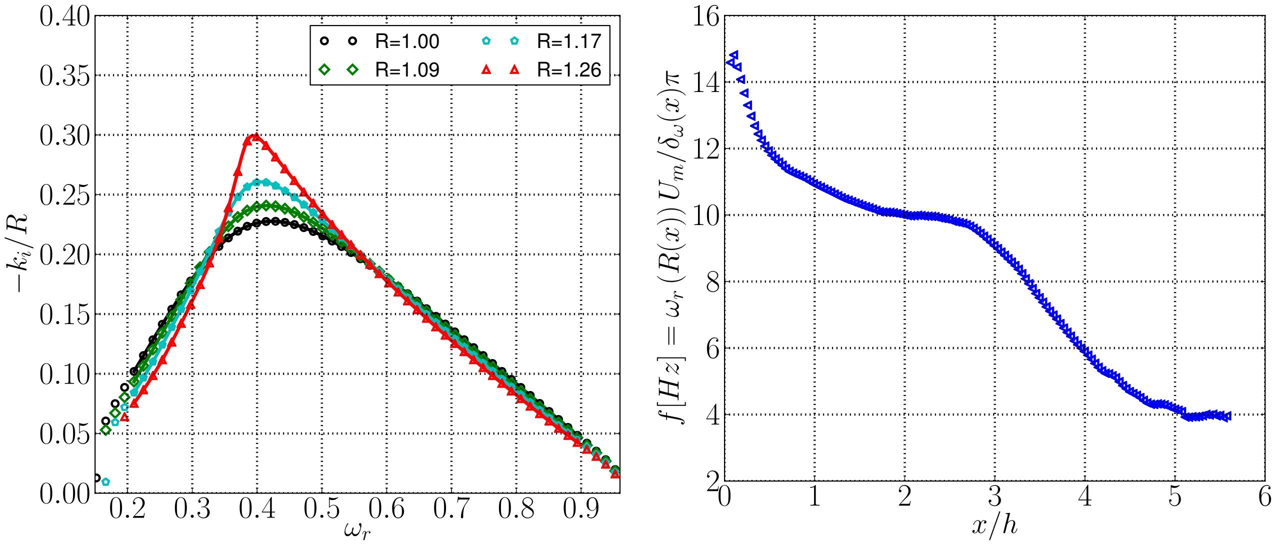

(c) Solution of the dispersion relation $\mathcal{D}(\omega, k, R)$. Maximum spatial growth rate ($-k_i(\max)$) occurs for $\omega(\max) \simeq 0.4$.

(d) The result $\omega_{\max}$ with the physical dimensions of the experiment is used to construct the selected natural frequency $f_n(x/h)$.

Fig. 7. Linear Stability analysis on experimental mean flow for the non-forced case, at $Re = 1520$. The selected frequency in (d) $f_n = 9.8Hz$ matches the Pitot measures.

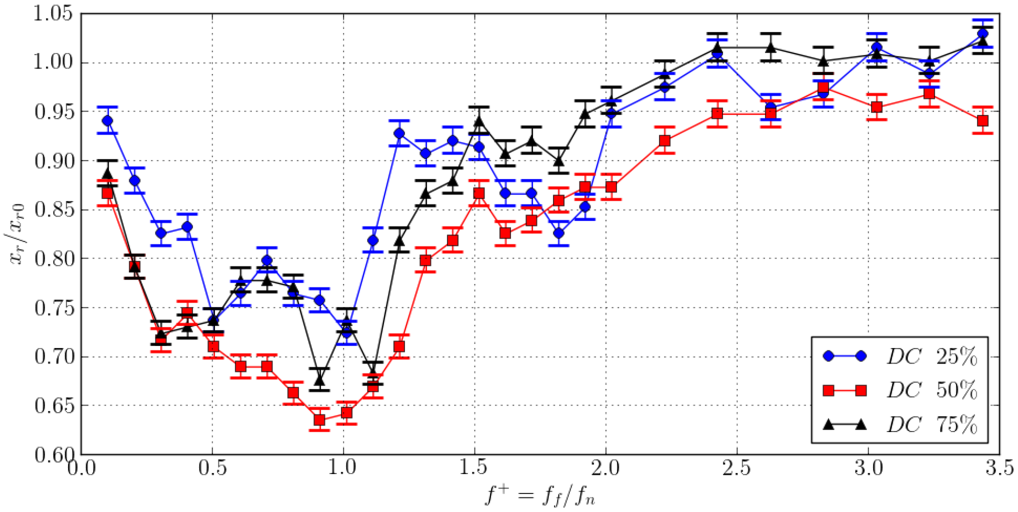

Fig. 8. Recirculation bubble length $x_r$ modifications under actuation for three forcing amplitudes and a range of frequencies $0.1 < f^+ < 3.4$.

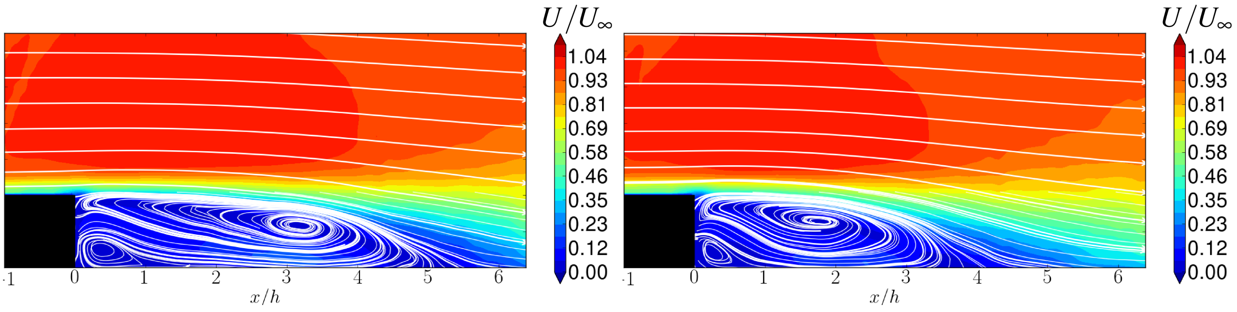

(a) DC 50% $f^+ \simeq 0.1$.

(b) DC 50% $f^+ \simeq 1$.

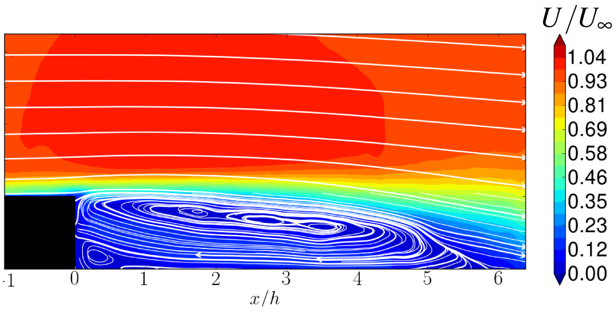

(c) DC 50% $f^+ \simeq 2.8$.

Fig. 9. Evolution of the mean flow, represented by contours of the non-dimensional velocity modulus $U/U_\infty$ and streamlines. Different forcing frequencies are considered.

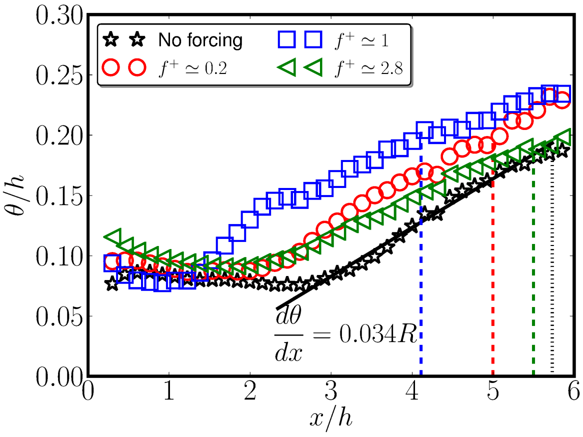

Fig. 10. Momentum thickness evolution downstream. Non-forced case and three forcing frequencies for a fixed forcing amplitude (%DC=25). Dashed lines show the corresponding recirculation length for each case.

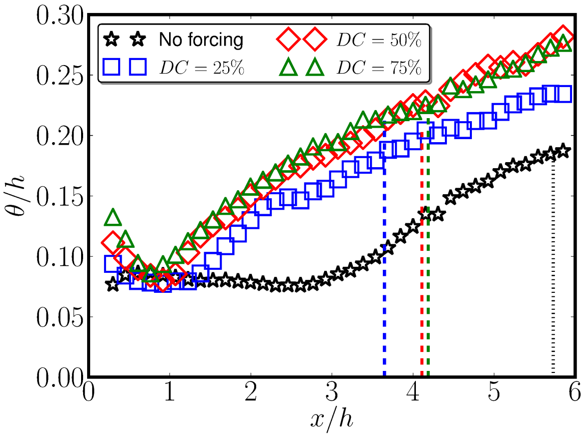

Fig. 11. Momentum thickness evolution downstream. Non-forced case and three forcing amplitudes for a fixed forcing frequency $f^+ = 1$.

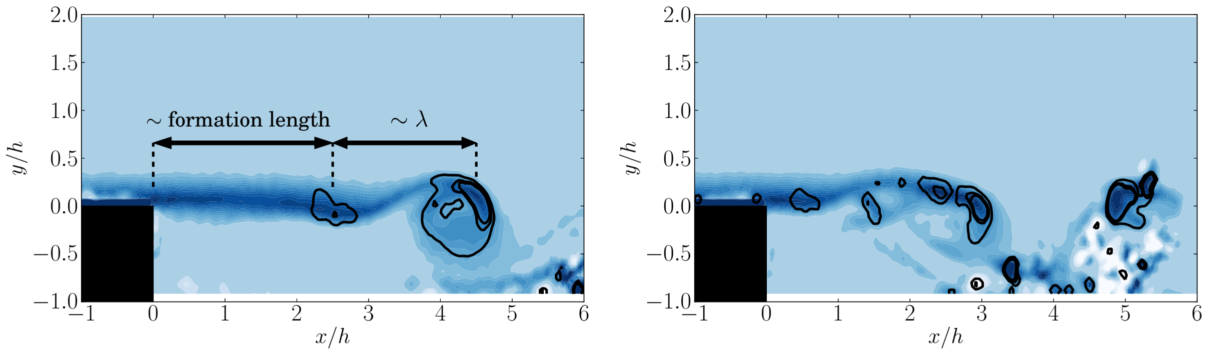

(a) Non forcing

(b) $f^+ \simeq 1$

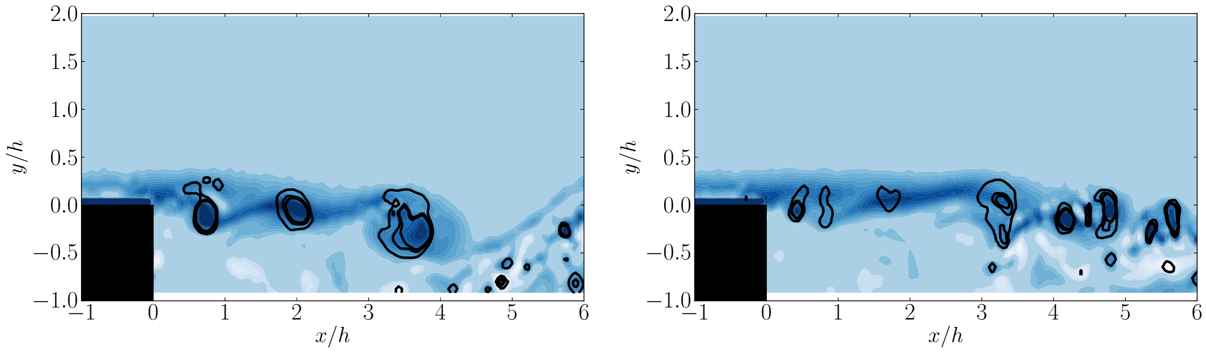

(c) $f^+ \simeq 0.5$

(d) $f^+ \simeq 1.8$

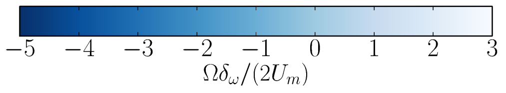

Fig. 12. Instantaneous vorticity contours for the natural flow and three forcing frequencies for $DC$=50%. Some $Q$ contours (solid lines) identify the main vortex of the flow. Formation length is appreciable as well as an approximate measure for the wavelength $\lambda$

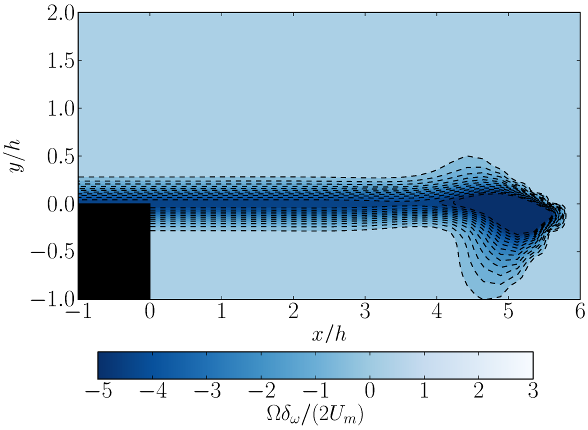

Fig. 13. Instantaneous vorticity contours for the more unstable mode of the linear stability problem for the non forced case. Experimental scales $\delta_\omega$ and $U_m$ are used on equation (7).

## List of Tables

| DC (%) | 25 | 50 | 75 |
|---|---|---|---|
| $G$ [cm$^2$/s] | 6.60 | 10.20 | 15.97 |
| $U_j/U_\infty$ | 0.13 | 0.20 | 0.35 |

Table 1. Flow rate induced by the ionic wind of the DBD device. A characteristic velocity for DBD jet is estimated for each $DC$.